Manuscript submitted to **Biophysical***Journal*

Article

The rotational diffusion of B-cell receptor *vs* antibody paratopes differentially affects their antigen binding kinetics

Miguel García-Sánchez[1], José Faro[2,3], and Mario Castro[1,*]

[1]Instituto de Investigación Tecnológica (IIT) and Grupo Interdisciplinar de Sistemas Complejos (GISC), Universidad Pontificia Comillas, Madrid, Spain

[2]Area of Immunology, Faculty of Biology, and Biomedical Research Center (CINBIO), Universidade de Vigo, Vigo, Spain

[3]Instituto Gulbenkian de Ciência, Oeiras, Portugal

[*]Correspondence: marioc@comillas.edu

ABSTRACT Since the pioneering works of Berg and Purcell, discriminating between diffusion followed by binding has played a central role in understanding cell signaling. B-cell receptors (BCR) and antibodies challenge that simplified view as binding to antigen follows after a chain of diffusion, rotations, tilts, and twists of their Fab arms due to their Y-shaped structure and flexibility. This paper analyzes the first-passage times due to these three rotations positioning the Fab arms in the proper position and orientation required for antigen binding. We combine analytical calculations with Brownian simulations to show that those times strongly depend on the dimensional physical conditions of the interactions (3-dimensional for free antigens and antibodies vs. 2-dimensional for membrane-anchored antigens and BCRs) and the flexibility and angle span between Fab arms of different immunoglobulin isotypes. Our quantitative estimations show that measuring kinetic binding rates using experimental methods in which the analyte is in solution hinders the underlying binding rates. As a consequence, the latter cannot generally be inferred from the former. This is highly relevant when one wants to relate BCR-antigen binding strength and B cell response, particularly during germinal center reactions. We argue that there is a need to revisit our current understanding of the BCR-antigen kinetic rates in germinal centers using state-of-the-art experimental assays.

SIGNIFICANCE 3-dimensional Ab-Ag effective affinity constants are unreliable surrogates for 2-dimensional BCR-Ag effective affinity constants.

INTRODUCTION

Antigen (Ag) binding to B-cell receptors (BCRs) can activate B lymphocytes, ultimately leading to their differentiation into antibody (Ab)-secreting plasma cells. While BCRs are membrane immunoglobulins (Ig)

linked to an invariant transmembrane heterodimer, Abs are soluble, Ig isoforms that lack the membrane-anchoring and transmembrane tail (1). The binding of BCRs and Abs to their cognate antigens is strongly influenced by the Ig structure (2). The basic structure of Igs consists of two identical polypeptide heavy (H) chains made of at least 3 globular domains, and two identical polypeptide light (L) chains made of 2 globular domains, with all Ig domains having a high aminoacid sequence homology between them. Each L chain is paired with the two N-terminal domains of a H chain, with covalent bonds that prevent their dissociation. The remaining domains of a H chain are paired with the corresponding domains of the other H chain, and are held together also by covalent bonds. In each H chain, the second domain is linked to the third one (starting from the N-terminal end) through an aminoacid sequence known as hinge region (1) (Figure 1a), which has a variable length specific to each Ig isotype. Igs are, thus, bivalent molecules with a typical Y shape, displaying two identical Ag-binding arms or fragments (Fab) that stem from a single constant arm (Fc). In contrast, to Abs, in a BCR each C-terminal domain of the Fc arm has a tail that spans the B cell membrane until the cytoplasm. Igs are flexible molecules thanks to the relative flexibility of the hinge region linking Fab arms to the Fc arm (3). This allows the two Fab arms to pivot independently of each other about the Fc region. Fab arms bind a small site named epitope (E) on an Ag through a small region of comparable size at the free Fab end known as paratope (P) (Figure 1a).

During a humoral immune response to protein Ags, B cells interact through their BCRs with their cognate Ag held in form of immunocomplexes on the membrane of specialized cell types, notably among them follicular dendritic cells (FDC) (4–6). This receptor-ligand interaction is similar to that of T-cell receptors (TCR) and their ligands, a complex of a protein-derived peptide with a molecule of the major histocompatibility complex (pMHC), in that it takes place in the context of a membrane-membrane interaction, and therefore in 2-dimensional (2D) conditions (7, 8). Yet, the effective kinetic rate constants and affinity constants of BCR-Ag interactions have not been measured until now, except for a couple of Abs (9, 10), due to a lack of adequate and easily implemented techniques. In contrast, for Ab-Ag interactions, which take place in 3D conditions, there are several techniques, particularly the so-called Surface Plasmon Resonance (SPR) assay, that are widely used to measure their effective kinetic rate constants and affinity constants, and traditionally it has been implicitly assumed that Ab-Ag interactions are a good proxy of BCR-Ag interactions.

We have shown before that, in general, protein-protein interactions can be described in detail by considering the three main sequential processes taking place in that interaction, namely: translational diffusion, rotational diffusion and molecular binding (7). In the case of BCR-Ag interactions (2D conditions) and Ab-Ag interactions (3D conditions) the translational *on* and *off* kinetic rates scale similarly to each other from 2D to 3D conditions (8). However, it is presently unknown whether the corresponding rotational *on* and *off* kinetic rates also scale similarly to each other from 2D to 3D conditions.

Here we perform a detailed analysis of BCR and Ab rotational rates in 2D and 3D conditions using the theory of stochastic narrow escape (11) and first passage processes (12), and combine analytical

calculations with Brownian simulations to provide a full quantitative picture of the first-passage times associated to the BCR and Ab rotational degrees of freedom. Our results show that the effective *on* and *off* kinetic rates of the Ig rotational diffusion process strongly depend on the physical conditions of the interactions (free antibodies and antigens *vs* BCRs and membrane-anchored antigens) and the flexibility and angle span between Fab arms of different Ig isotypes. This implies that, contrary to the traditional implicit assumption, the kinetics of BCR-Ag interactions cannot be inferred, in general, from those of Ab-Ag interactions.

A FIRST-PASSAGE-TIME FORMALISM OF THE ROTATIONAL DIFFUSION STEPS DURING BCR AND ANTIBODY BINDING TO ANTIGEN

The three-step description of kinetic binding

In general, the kinetics of reversible protein-protein interactions consist of three generic processes (mostly occurring sequentially). The first one, translational diffusion, comprises the spatial approximation of R and L molecules to a distance that allows binding; we denote this *close-enough* by RL^*. In the second step, rotational diffusion, the two close molecules must attain a proper orientation to be able to bind each other; we denote this close and oriented state as RL (in the case of Igs, a paratope has to be properly oriented for binding its epitope). Once properly oriented, they can form a bound complex C (7). Equation (1) summarizes these series of states and processes,

$$R + L \underset{k_d^-}{\overset{k_d^+}{\rightleftharpoons}} RL^* \underset{e^-}{\overset{e^+}{\rightleftharpoons}} RL \underset{k^-}{\overset{k^+}{\rightleftharpoons}} C \tag{1}$$

where k_d^+, k_d^- are, respectively, translational diffusion *on* and *off* rate constants, e^+ and e^- are diffusion *on* and *off* rate constants for effective or global rotation, and k^+ and k^- are the intrinsic or molecular *on* and *off* rate constants. It is worth noting that De Lisi (14) already emphasized the relevance of this three-step analysis generalizing the diffusion only plus binding framework pioneered by Berg and Purcell (15).

Traditionally, binding has been analyzed experimentally lumping together those three steps assuming they occur in a single step. The *effective* kinetic rates for this simplified view can be formally derived by assuming a quasi-steady state approximation for the intermediate states $[RL^*]$ and $[RL]$, which leads to the following expressions for k_{eff}^+ and k_{eff}^- (7):

$$k_{\text{eff}}^+ = \left.\frac{k_d^+\, e^+\, k^+}{k_d^-\, e^- + k^+(k_d^- + e^+)}\right|_{3D/2D} \tag{2}$$

$$k_{\text{eff}}^- = \left.\frac{k_d^-\, e^-\, k^-}{k_d^-\, e^- + k^+(k_d^- + e^+)}\right|_{3D/2D} \tag{3}$$

where the subscripts $3D/2D$ denote that the translational and global rotational diffusion rate constants are those corresponding to either 3D or 2D reactions. Note that k^+ and k^- are independent of the dimensional

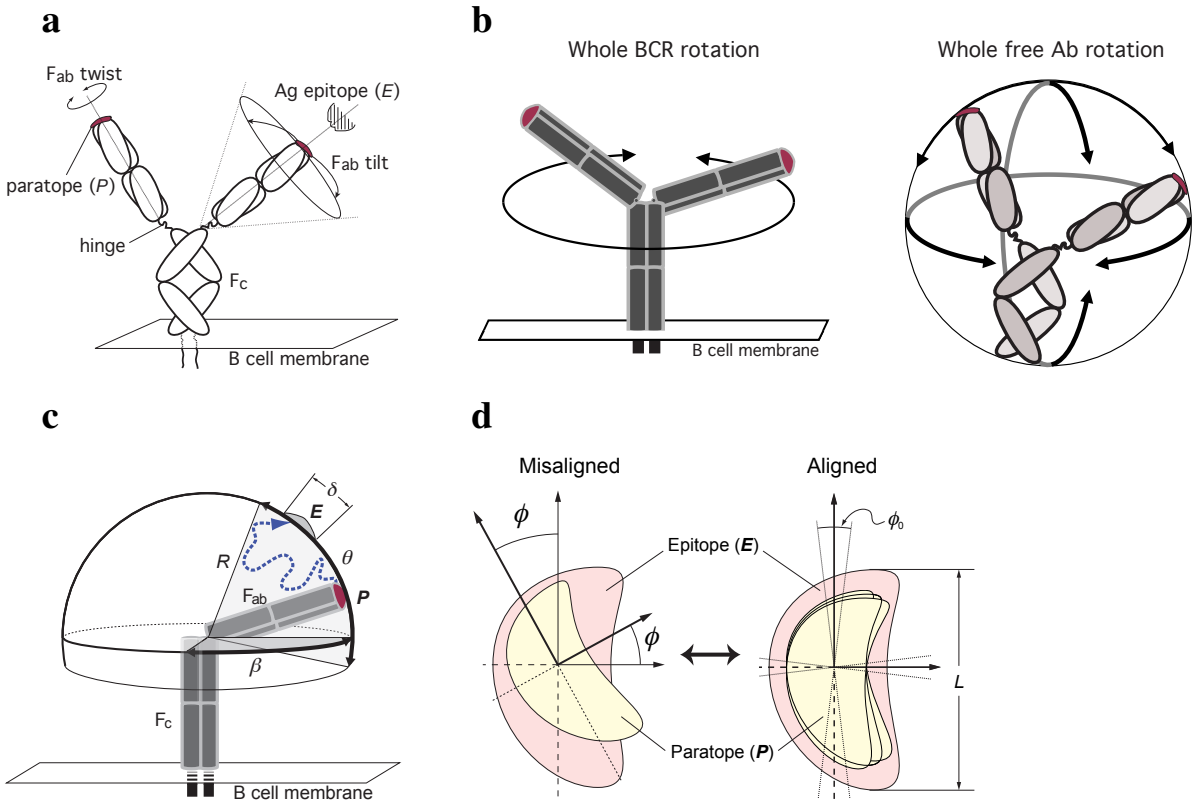

Figure 1: Possible Ig rotations impacting on the position of a paratope P relative to an Ag epitope E (the relative proportions of the paratope, epitope, Fc and Fab arms are not at scale). **a**. The position of each paratope in an Ig (whether mIg or free Ab) is submitted to two possible Fab rotations, Fab tilt (wagging and wobbling) that affects independently each Fab arm (depicted on the right side), and Fab twist in which each Fab arm rotates, independently of each other, along its major axis (from the hinge region to P; depicted on the left side). The speed of these two Fab rotations might differ in a BCR and a free Ab. **b**, In addition to Fab rotations, the position of each paratope is affected by the rotation of the whole Ig. Left side depicts whole mIg (BCR) rotation, mostly restricted to a rotation along the Fc axis. Right side depicts whole free Ab rotation, which is unrestricted in the three spatial dimensions. **c**, Sketch of the diffusion of P due to Fab tilt, assuming the epitope is in a fixed position; this movement is constrained to a spherical cap on a sphere of radius R = length of a Fab arm ≈ 84 Å (13) and to Fab altitude and azimuth angles θ and β, respectively. Depicted is a possible path followed by paratope P toward epitope E (dotted line). The angle δ corresponds to an arc on the spherical surface equal to the major length of E. For clarity, the outlined mIg is depicted with only one Fab arm. **d**, Alignment or misalignment of P and E due to Fab twist. P rotates with variable angle ϕ relative to E (left side). Such rotation will align or misalign P and E, allowing or impeding their chemical binding. For aligned P and E there is a tolerance angle, ϕ_0, within which the chemical reaction can proceed (right side). The view in panel **d** is along the major Fab axis.

condition and, thus, are identical in 3D and 2D interactions. The divisor in these equations determine a threshold for k^+,

$$k^+_{\text{threshold}} = \frac{k^-_d \; e^-}{k^-_d + e^+} \tag{4}$$

such that for $k^+ > k^+_{\text{threshold}}$, k^+_{eff} approaches asymptotically a plateau given by $k^+_{\text{plateau}} = \frac{k^+_d \; e^+}{k^-_d + e^+}$, and k^-_{eff}

becomes proportional to the dissociation affinity constant (8).

But even this three-step process can be further analyzed to capture the subtle —yet crucial—role of the Y structure of BCRs and Abs. In particular, the wagging and wobbling movements of Ig Fab arms relative to the Fc arm, made possible by the hinge region of the Ig heavy chains, determine the position of the corresponding paratopes relative to the Fc arm and are referred to here as tilt rotation of paratopes or Fab tilt (Figures 1a and c) (3, 16, 17). This rotation is characterized by *on* and *off* rate constants, hereby denoted e_t^+ and e_t^-, respectively. In addition, a Fab arm can twist about its major axis thanks again to the relative flexibility of the hinge segment (18, 19). This Fab twisting affects the orientation or alignment of a paratope relative to an epitope on a relatively immobile Ag molecule tethered to an FDC membrane. We refer to this rotation as alignment rotation (Figures 1a and d) and the *on* and *off* rate constants characterizing this rotation are denoted, respectively, e_a^+ and e_a^-. Last, the possible rotation of the whole BCR about the Fc axis or the rotation of an Ab in solution as a whole (Figure 1b) contributes to the global paratope rotation with *on* and *off* rate constants denoted e_w^+ and e_w^-, respectively. Due to such complex combination of different rotational diffusion modes affecting the relative position of paratopes of BCRs and free Abs, the above-mentioned global rate constants e^+ and e^- are, in fact, compound quantities of the more elemental rates characterizing the whole molecule, Fab tilt and alignment rotations.

The global *on* rotation takes place in two steps. First, a Fab paratope P becomes close enough to an epitope E through whole Ig and Fab tilt rotation, and then P and E become correctly oriented by a twist or alignment rotation. The first step, the close approaching of P and E, is a combination of the whole molecule and Fab tilt rotation processes taking place in parallel or in any temporal order. Hence its rate is the sum of the two individual processes, $e_{w+t}^+ = e_w^+ + e_t^+$, and thus the corresponding mean time is given by $t_{w+t} = \frac{1}{e_{w+t}^+}$. However, the *on* alignment rotation follows *sequentially* after the approaching of P and E, hence the mean rotation time of the two steps (approaching and alignment) is the sum of their respective mean times, that is, $t_{on} = t_{w+t} + t_a$ and, consequently, $\frac{1}{e^+} = \frac{1}{e_{w+t}^+} + \frac{1}{e_a^+}$. At variance with e^+, the global *off* rotation rate, e^- (*i.e.*, from the RL state to the RL^* state), is determined by the *whole* and *tilt* off rotations, which can take place in *parallel* or in any temporal order. This can be described in terms of a reaction scheme as:

$$\cdots \rightleftharpoons RL^* \underset{e_{w+t}^-}{\overset{e_{w+t}^+}{\rightleftharpoons}} [RL] \underset{e_a^-}{\overset{e_a^+}{\rightleftharpoons}} RL \rightleftharpoons \cdots \qquad (5)$$
$$RL^* \xleftarrow{\quad e_{w+t}^- \quad} RL$$

And according to the above:

$$e^+ = \frac{e_{w+t}^+ \times e_a^+}{e_{w+t}^+ + e_a^+} \qquad \text{and} \qquad e^- = e_{w+t}^-. \qquad (6)$$

Mathematical derivation of the rotational rates

Due to thermal fluctuations, proteins diffuse randomly, driven by molecular collisions or vibrations until that motion stops by reaching a binding site. Hence, we model the rotational tilt diffusion combined with the whole rotation of the Fc region as a Brownian motion of the paratope on a spherical surface, that terminates when it reaches the epitope. Similarly, the rotational alignment step can be represented as a Brownian motion of the paratope in a circumference which terminates when it acquires an adequate orientation, that is, an angle orientation that allows binding. According to the theory of stochastic narrow escape (11) and first-passage processes (12), the mean first passage time (MFPT) until absorption of a Brownian particle inside a domain Ω, with absorbing $\partial\Omega_a$ and reflecting $\partial\Omega_r$ boundaries, satisfies the following mixed boundary value problem:

$$\begin{cases} D\Delta\tau(x) = -1, \quad x \in \Omega, & \text{(7a)} \\ \tau(x) = 0, \quad x \in \partial\Omega_a, & \text{(7b)} \\ \dfrac{\partial\tau(x)}{\partial n(x)} = 0, \quad x \in \partial\Omega_r, & \text{(7c)} \end{cases}$$

where D is the diffusion coefficient and $\mathbf{n}$ is the unit outer normal vector to the boundary. The MFPT $\tau(x)$ is dependent on the initial position x and the size of the absorbing domain Ω_a, which in our case is determined, for the tilting step, by the angle δ corresponding to the epitope length, and, for the alignment step, by the angle range of adequate orientations ϕ_0. From now on, we will be referring to $\tau(x,\delta)$ or $\tau(x,\phi_0)$ as the MFPT and $\tau(\delta)$ as the global MFPT. The inverse of $\tau(\delta)$ is the desired on/off-rate and results from averaging over all possible initial positions. We summarize the domains and notations associated with each process in Table 1 where we also include a column pointing to the analytical solution of each sub-problem.

The angles δ and ϕ_0 are those defined in Figures 1c and 1d. The tolerance deviation angle, ϕ_0, has been estimated to be in the range $5°(\equiv 0.087 \text{ rad}) < \phi_0 < 11°(\equiv 0.192 \text{ rad})$ (20). To estimate δ, we consider the spherical surface with radius $R \approx 84$ Å defined by a Fab arm (13, 21). On this surface, an epitope with length $L = 28$ Å (22) defines a maximum angle $\delta \approx 19°(\equiv 0.332 \text{ rad})$.

Aligment rotational e_a^+ and e_a^-

The *off* and *on* alignment rates, denoted here, respectively, e_a^- and e_a^+, are in principle independent of the 2D and 3D conditions. For the off-rate process, the particle representing a twisting paratope diffuses within a range or arc of adequate orientations $\Omega^- = [0, \phi_0]$ until it loses a proper alignment through the boundaries $\partial\Omega_a^- = \{0, \phi_0\}$. Whereas, in the on-rate process, the paratope diffuses inside an arc $\Omega^+ = [0, 2\pi - \phi_0]$ until it acquires an adequate alignment through the boundaries $\partial\Omega_a^+ = \{0, 2\pi - \phi_0\}$. Denoting $\phi_- = \phi_0$ and $\phi_+ = 2\pi - \phi_0$, the mixed boundary value problems for the associated MFPTs $\tau_a^\pm$ are:

Table 1: Description and geometry of the domains (Ω), absorbing domains (Ω_a) and reflecting boundaries ($\partial\Omega_r$)) for binding and unbinding processes in B-cell receptors and free Antibodies. (+) denote *on-rate* and (−), *off-rate*.

Step[a]	Notation	Ω	$\partial\Omega_a$ Ω_a	$\partial\Omega_r$	**Eqn.**
Fab Aligment (+)	$e_a^+(\phi_0)$	Arc $(\phi_0, 2\pi)$	Arc $[0, \phi_0]$	—	(11)
Fab Aligment (−)	$e_a^-(\phi_0)$	Arc $(0, \phi_0)$	Arc $[\phi_0, 2\pi]$	—	(12)
Ab+Fab rotation (+)	$e_{t+w}^{3D+}(\delta)$	Spherical cap $(\pi - \delta)$	Spherical cap (δ)	—	(18)
Ab+Fab rotation (−)	$e_{t+w}^{3D-}(\delta)$	Spherical cap (δ)	Spherical cap $(\pi - \delta)$	—	(22)
BCR+Fab rotation (+)	$e_{t+w}^{2D+}(\delta)$	Portion of Sphere	Spherical cap (δ)	$\theta \in \{\theta_{\min}, \theta_{\max}\}$ $\beta \in \{0, \pi\}$	(26)
BCR+Fab rotation (−)	$e_{t+w}^{2D-}(\delta)$	Spherical cap (δ)	Spherical cap $(\pi - \delta)$	—	(27)

[a] *On* and *off* rates are indicated, respectively, with (+) and (–).

$$\begin{cases} D\Delta\tau_a^{\pm}(\theta, \phi_0) = -1, \quad 0 < \theta < \phi_{\pm}, & \text{(8a)} \\ \tau_a^{\pm}(0) = 0, & \text{(8b)} \\ \tau_a^{\pm}(\phi_{\pm}) = 0. & \text{(8c)} \end{cases}$$

Problem (8) can be solved through direct integration:

$$\tau^{\pm}(\theta, \phi_0) = \frac{1}{2D}\theta \cdot (\phi_{\pm} - \theta). \tag{9}$$

Averaging Eqn. (9) over all initial positions $\theta \in [0, \phi_{\pm}]$ yields the global MFPTs:

$$\tau_a^{\pm}(\phi_0) = \frac{\displaystyle\int_0^{\phi_{\pm}} \theta\tau^{\pm}(\theta, \phi_0)d\theta}{\displaystyle\int_0^{\phi_{\pm}} \theta d\theta} = \frac{\phi_{\pm}^2}{12D}. \tag{10}$$

The corresponding *on* and *off* rates are given by the equations:

$$e_a^+(\phi_0) = \frac{12D}{(2\pi - \phi_0)^2}, \tag{11}$$

$$e_a^-(\phi_0) = \frac{12D}{\phi_0^2}. \tag{12}$$

where $D \equiv D_a$.

Figure 2 shows a comparison between the times $\tau_a^{\pm}(\phi_0)$ computed through Monte-Carlo simulations and the times obtained using the explicit solutions given by Eqn. (10).

3D rotational rates of Abs

For the on-rate $e_{t+w}^{3D+}(\delta)$, the particle representing the paratope diffuses throughout the spherical surface until it encounters the epitope represented by a spherical patch of angle δ (Fig. 3a). By setting the epitope

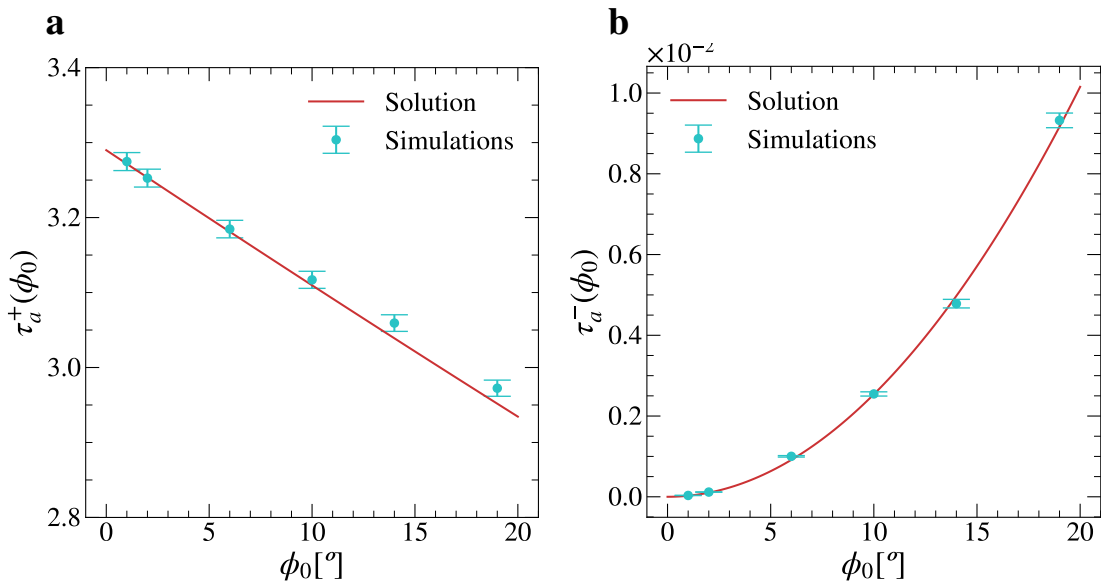

Figure 2: **Comparison between numerical calculations and explicit solutions for rotational alignment** (given by Eqs. (10)) of the global MFPTs $\tau_a^+(\phi_0)$ (**a**) and $\tau_a^-(\phi_0)$ (**b**). Parameters in **a** and **b** for each value of ϕ_0: $dt = 10^{-5}$, $D = 1$, # initial positions = 500, # repetitions per initial position = 2000.

at the south pole of the sphere, we can see that the MFPT until absorption is symmetrical in the azimuthal angle β, $\tau_{t+w}^{3D+}(\theta,\beta,\delta) \equiv \tau_{t+w}^{3D+}(\theta,\delta)$. The mixed boundary value problem (7) is, then, given by:

$$\begin{cases} D\Delta\tau_{t+w}^{3D+}(\theta,\delta) = -1, \quad 0 < \theta < \theta_{\max}^{+} = \pi - \delta/2, & \text{(13a)} \\ \tau_{t+w}^{+}(\theta_{\max}^{+}) = 0, & \text{(13b)} \end{cases}$$

Note that for the off-rate, $e_{t+w}^{3D-}(\delta)$, the particle diffuses inside a polar cap of angle δ (see Fig. 3b). Thus, the mixed boundary problem for $\tau_{t+w}^{3D-}(\theta,\delta)$ is equivalent to Eqn. (13) but with the boundary set at $\theta_{\max}^{-} = \delta/2$, that is:

$$\begin{cases} D\Delta\tau_{t+w}^{3D-}(\theta,\delta) = -1, \quad 0 < \theta < \theta_{\max}^{-} = \delta/2, & \text{(14a)} \\ \tau_{t+w}^{-}(\theta_{\max}^{-}) = 0, & \text{(14b)} \end{cases}$$

Problems defined by Eqns. (13-14) can be solved by direct integration. For that, applying the change of variable $r = \sin\theta$ and substituting the Laplace operator in spherical coordinates yields:

$$D\Delta\tau_{t+w}^{3D\pm}(r,\delta) = \frac{\sqrt{1-r^2}}{r}\frac{\partial}{\partial r}\left(r\sqrt{1-r^2}\frac{\partial}{\partial r}\right)\tau = -1, \Longleftrightarrow \frac{\partial\tau_{t+w}^{3D\pm}(r,\delta)}{\partial r} = \frac{1}{r} + \frac{C_1}{r\cdot\sqrt{1-r^2}}, \Longleftrightarrow$$
$$D\tau_{t+w}^{3D\pm}(r,\delta) = \log r + \frac{C_1}{2}\log\left(\frac{1-\sqrt{1-r^2}}{1+\sqrt{1-r^2}}\right) + C_2.$$

Substituting back r by $\sin\theta$ gives the equation:

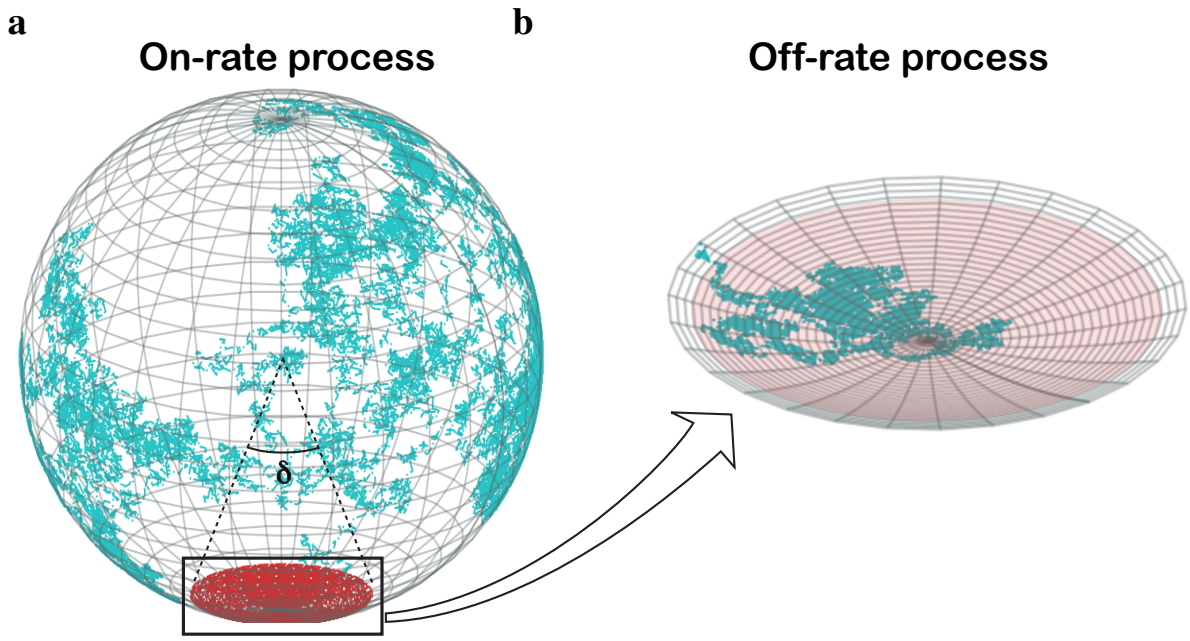

Figure 3: **Random Walk view of Ab's paratope diffusion in 3D. a**, On-rate process: The paratope (blue) diffuses on the sphere until finding the epitope (red). δ, angle of the arc with length equal to the major length of the epitope. **b**, Off-rate process: The paratope diffuses within the epitope area (pale red) until escape (grey area).

$$D\tau_{t+w}^{3D\pm}(\theta,\delta) = \log(\sin\theta) + \frac{C_1}{2}\log\left(\frac{1-\cos\theta}{1+\cos\theta}\right) + C_2. \tag{15}$$

The value of C_2 is obtained from the absorbing boundary condition at $\theta_{\max}^{\pm}$, and thus:

$$\tau_{t+w}^{3D\pm}(\theta,\delta) = \frac{1}{D}\left[\log\left(1+\cos\theta\right) - \log\left(1-\cos\theta_{\max}^{\pm}\right)\right] \tag{16}$$

A comparison of the simulated MFPT $\tau_{t+w}^{3D\pm}(\theta,\delta)$ with its exact value given by Eqn. (16) is shown in Fig. 4. Finally, averaging Eqn. (16) over all possible initial positions $\theta \in [0,\theta^{\pm}]$ gives the following expression for the global MFPT:

$$\tau_{t+w}^{3D\pm}(\delta) = \frac{1}{D}\left[\csc^2\left(\frac{\theta_{\max}^{\pm}}{2}\right)\left(\log(2) - \log\left(\cos\left(\theta_{\max}^{\pm}\right)+1\right)\right) - 1\right] \tag{17}$$

and, thus, the associated mean *on*-rate follows the equation:

$$e_{t+w}^{3D+}(\delta) = \frac{2\,D_{t+w}}{\sec^2\left(\frac{\delta}{4}\right)\left[\log(2) - \log\left(1+\cos\frac{\delta}{2}\right)\right] - 1}, \tag{18}$$

where $D \equiv D_{t+w} \approx D_t + D_w$.

For the *off*-rate $e_{t+w}^{3D-}(\delta)$, since the angle size of the epitope is relatively small ($\delta \approx 19°$), we can approximate the off-rate taking the limit $\delta \to 0$. In this limit, the epitope can be considered as a disk of radius $R = \sin\delta/2$, thus the problem for the mean first passage time $t_{t+w}^{3D-}(\sin\theta,\delta)$ is:

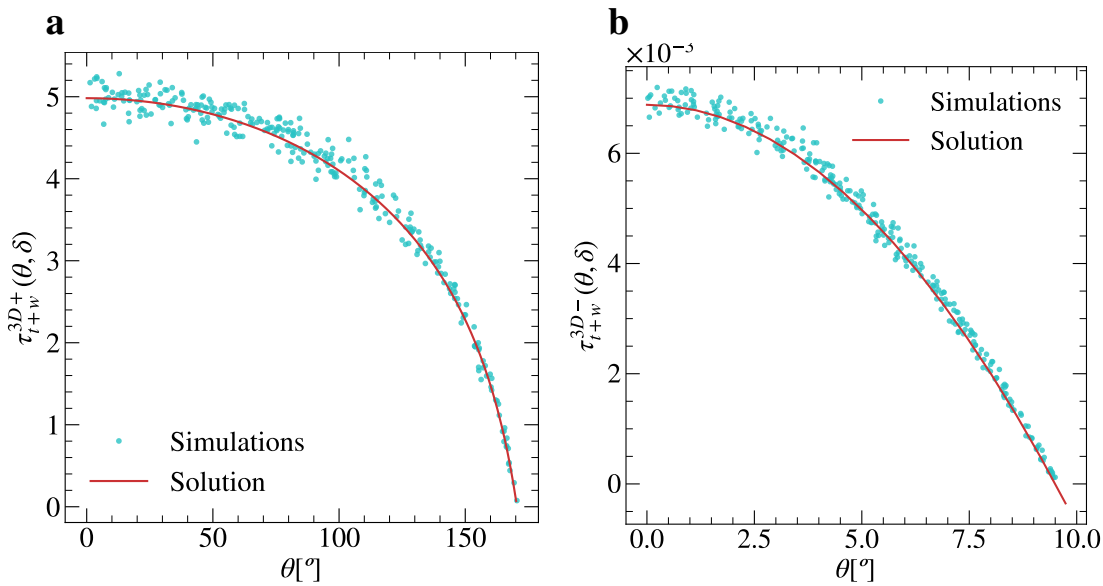

Figure 4: **Comparison between MFPT numerical calculations and explicit solutions for 3D whole Ab and Fab tilt rotations**. **a, b** Comparison between simulated $\tau^{3D\pm}_{t+w}(\theta,\delta)$ (blue) and their explicit solution, Eqn. (16). Parameters: $\delta = 19°$; $dt = 10^{-5}$ (**a**), $dt = 10^{-6}$ (**b**); # initial positions = 300; # simulations per initial position = 1000.

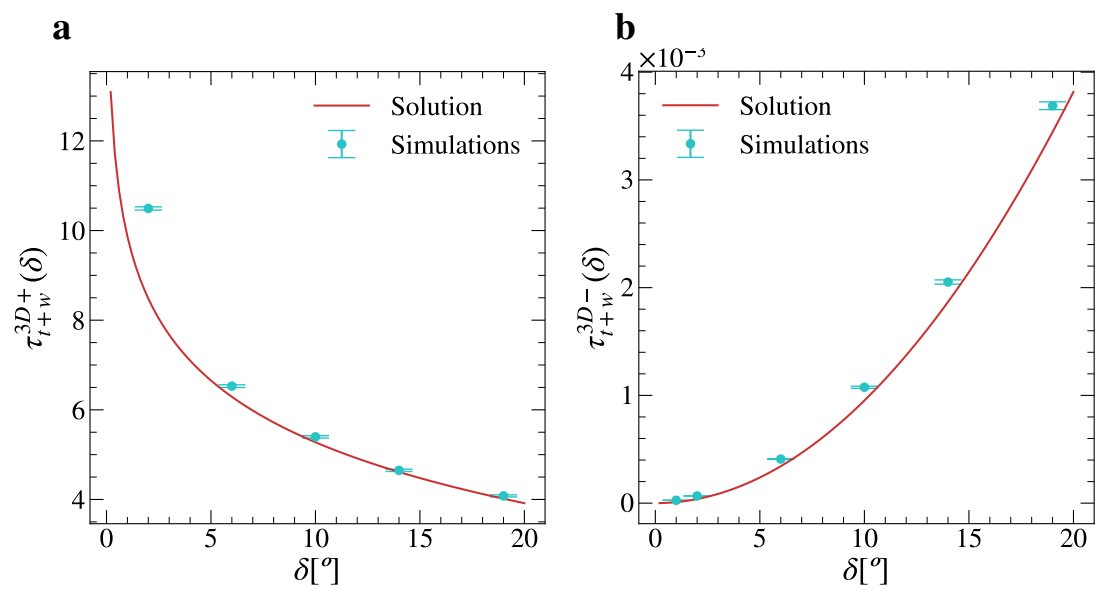

Figure 5: **Comparison between global MFPT numerical calculations and explicit solutions for 3D whole Ab and Fab tilt rotations**. **a, b** Comparison between simulated $\tau^{3D\pm}_{t+w}(\delta)$ (blue) and their explicit solutions, Eqns. (17,21). Parameters in **a** for each value of δ: $dt = 2e-4$, $D = 1$, # initial positions = 3000, # repetitions per initial position = 100. Parameters in **b** for each value of δ: $dt = 1e-5$, $D = 1$, # initial positions = 3000, # repetitions per initial position = 1000.

$$\begin{cases} D\Delta\tau^{3D-}_{t+w}(\sin\theta,\delta) = -1, \quad 0 < \sin\theta < \sin\delta/2, & \text{(19a)} \\ \tau^{3D-}_{t+w}(\sin\delta/2) = 0. & \text{(19b)} \end{cases}$$

Applying the change of variable $r = \sin\theta$, Eqn. (19) yields:

$$D\Delta\tau_{t+w}^{3D-}(r,\delta) = \frac{\partial}{\partial r}\left(r\frac{\partial}{\partial r}\right)\tau^{3D-}(r,\delta) = -1, \Longleftrightarrow \frac{\partial\tau^{3D-}(r,\delta)}{\partial r} = -\frac{r^2}{4} + C_1, \Longleftrightarrow$$
$$D\tau_{t+w}^{3D-}(r,\delta) = -\frac{r^2}{2} + C_1\log(r) + C_2.$$

From the condition of finitude at $r = 0$, it follows that $C_1 = 0$, and from the absorbing boundary condition it follows C_2, which yields:

$$\tau_{t+w}^{3D-}(r,\delta) = \frac{1}{4D}\left(R^2 - r^2\right). \tag{20}$$

Averaging over the initial position $r \in [0, R]$ gives the global MFPT:

$$\tau_{t+w}^{3D-}(\delta) = \frac{\int_0^R r\tau_{t+w}^{3D-}(r,\delta)dr}{\int_0^R rdr} = \frac{R^2}{8D} = \frac{\sin^2\delta/2}{8D}, \tag{21}$$

and, therefore, the corresponding approximated off-rate is:

$$e_{t+w}^{3D-}(\delta) \approx \frac{8D}{\sin^2\delta/2}. \tag{22}$$

with $D \equiv D_{t+w}$.

A comparison of the simulated global MFPT $\tau_{t+w}^{3D\pm}(\delta)$ with its exact value given by Eqns. (17, 21) is shown in Fig. 5.

2D compound tilt+whole molecule rotational rates of BCRs

In BCRs, the anchoring to the cell membrane has two main effects in the seek of epitope by the paratopes. First, its whole rotation motion is restricted to essentially the axis normal to the cell membrane in a highly crowded molecular environment. Although the exact value of the rotational diffusion coefficient $D_w(2D)$ has not been experimentally determined, one can take as a reference value that of the epidermal growth factor receptor (23), which is of the order 10^3 rad$^2/s$. This is three orders of magnitude smaller that the $D_t(2D)$ (Table 3). Second, the domain Ω that the paratopes cover is determined by the Fab tilt flexibility. The different Ig isotypes and subclasses in human and mouse have different hinge regions and, consequently, they differ substantially in flexibility and tilt rotation. The flexibility in the polar angle θ, i.e, the flexibility of the Fab arms with respect to the Fc region, is well characterized. In particular, human IgG subclasses can be ordered in decreasing flexibility as: IgG3 > IgG1 > IgG4 > IgG2 (3). In total agreement with the reported functional equivalence between mouse and human IgGs (see Table 2) murine

IgG subclasses can be similarly ordered as: IgG2b > IgG2a > IgG1 > IgG3 (24). Contrary, the flexibility in the azimuthal angle β is not well characterized. Nevertheless, based on the study of Zhang *et al* (25) that analyzed the conformational flexibility of IgG1 antibody molecules using individual particle electron tomography, one can argue that each paratope can cover a 180° range in the azimuthal angle. Thus, the total domain covered by both paratopes is $\Omega = \{(\theta, \beta)|\ \theta \in [\theta_{\min}, \theta_{\max}], \beta \in [0, 2\pi]\}$. Furthermore, since $D_t(2D) \gg D_w(2D)$, we can neglect the marginal effect of the whole rotation motion, i.e $\tau_{t+w}^{2D\pm} \approx \tau_t^{2D\pm}$. In this approximation, each paratope covers one half of Ω, namely $\Omega_1 = \{(\theta, \beta)|\ \theta \in [\theta_{\min}, \theta_{\max}], \beta \in [0, \pi]\}$ and $\Omega_2 = \{(\theta, \beta)|\ \theta \in [\theta_{\min}, \theta_{\max}], \beta \in [\pi, 2\pi]\}$. For simplicity, we will suppose that the epitope is completely contained in either Ω_1 or Ω_2 and thus we only need to consider one of both paratopes (see Fig. 6).

Table 2: **Empirical estimates of the tilt angle ranges of murine and human immunoglobulins.** Note the agreement between the reported Fab-Fc tilt θ angles[c] of mouse and human IgG subclasses.

Functional equivalence[a]				
Mouse	**Human**	**Fab-Fab angles**[b]	**Fab-Fc angles**[b]	θ^c
IgG2b	IgG3	(83° — 189°)	(50° — 122°)	72°
IgG2a	IgG1	(74° — 160°)	(77° — 137°)	60°
IgG1	IgG4	(89° — 167°)	(73° — 123°)	50°
IgG3	IgG2	(95° — 159°)	(67° — 131°)	64°
IgM	IgM	(49° — 161°)		
IgD	IgD	(65° — 219°)		

[a] Data from references (26, 27).

[b] Range values compiled from references (3, 17).

[c] Calculated as the difference of angles in the range of Fab-Fc angles (see Figure 1c).

Note that in this situation the MFPT depends on the initial position of the paratope (θ, β), and the position and size of the epitope $(\theta_{\text{epi}}, \beta_{\text{epi}}, \delta)$. Through Monte-Carlo simulations, we computed the global MFPT $\tau_t^{2D+}(\theta_{\text{epi}}, \beta_{\text{epi}}, \delta)$ for the different IgGs subclasses, multiple values of $\delta = \{19°, 14°, 10°, 6°, 2°\}$ and different positions of θ_{epi}, keeping $\beta_{\text{epi}} = 90°$. As it can be seen in Fig. 7, the global MFPTs of the IgGs subclasses differ significantly from one to another, being more notorious between the IgG2b and IgG1 subclasses. Interestingly, the difference between IgGs subclasses increases as the size of the paratope δ decreases. These results show that the same paratope in different Ab classes might result in different rotation rate constants and, therefore, in different effective rate constants, besides any differences imposed by Ig class-specific glycosylation (13, 28).

The exact solution of the system of Eqns. (7) for the MFPT $\tau_t^{2D+}(\theta, \beta, \theta_{\text{epi}}, \beta_{\text{epi}}, \delta)$ requires the knowledge of the pseudo-Green functions for the domains in Fig. 6 that, to our knowledge cannot be obtained using closed mathematical expressions. To overcome this limitation, here we use a variational

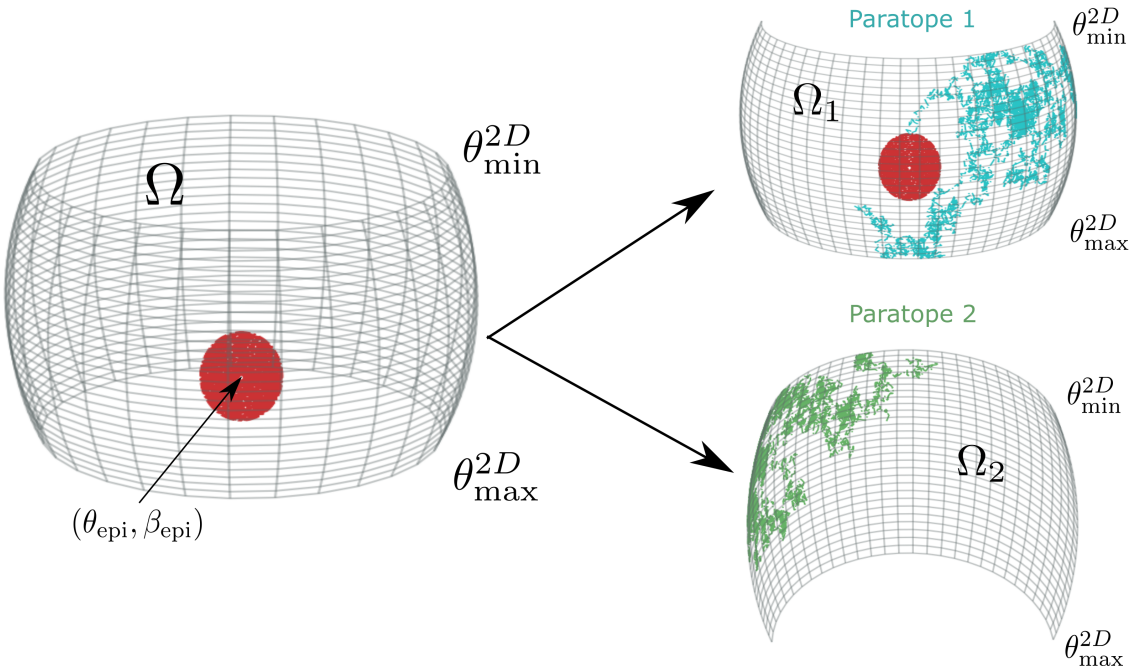

Figure 6: **Spatial constraints for BCRs paratope tilt rotation**. Neglecting the whole rotation motion, each paratope of the BCR covers only one half (Ω_1 and Ω_2) of the whole domain $\Omega = \Omega_1 \bigcup \Omega_2$. If the epitope is completely contained in Ω_1 or Ω_2 only one paratope contributes to the search of the epitope.

method: we will consider the case where the epitope is at the north pole of the sphere and the Fab tilt is only limited in southern regions and leave one free parameter to improve the accuracy of the approximation. In the latter situation, the MFPT only depends on the size of the epitope δ and the initial position $\theta \in [\delta/2, \hat{\theta}_{\max}]$, where $\hat{\theta}^{2D}_{\max}$ is the *variational angle* that should be related with the arc length $\theta_c = \theta^{2D}_{\max} - \theta^{2D}_{\min}$ of the original problem. In Fig. 8a we show the remarkble agreement between the variational approximation and the numerical simulations. The mixed boundary value problem for the MFPT $\tau_t^{2D+}(\theta, \delta)$ is defined by the set of equations (7) but applied to τ_t^{2D+}:

$$\begin{cases} D\Delta\tau_t^{2D+}(\theta,\delta) = -1, \quad \delta/2 < \theta < \hat{\theta}_{\max}, & \text{(23a)} \\ \tau_t^{2D+}(\delta/2) = 0, & \text{(23b)} \\ \left.\dfrac{\partial \tau_t^{2D+}(\theta)}{\partial\theta}\right|_{\hat{\theta}_{\max}} = 0. & \text{(23c)} \end{cases}$$

Problem (23) has the same structure as problem (13) with the addition of the reflecting boundary condition at $\hat{\theta}_{\max}$. Applying the boundary conditions, Eqns. (17b-c) gives the solution:

$$\tau_t^{2D+}(\theta,\delta) = \frac{1}{D}\log\left(\frac{\sin\theta}{\sin\delta/2}\right) + \frac{\cos\hat{\theta}_{\max}}{2}\left(\log\frac{\tan^2\delta/4}{\tan^2\theta/2}\right). \tag{24}$$

Averaging over the initial positions $\theta \in [\delta/2, \hat{\theta}_{\max}]$ gives the global MFPT:

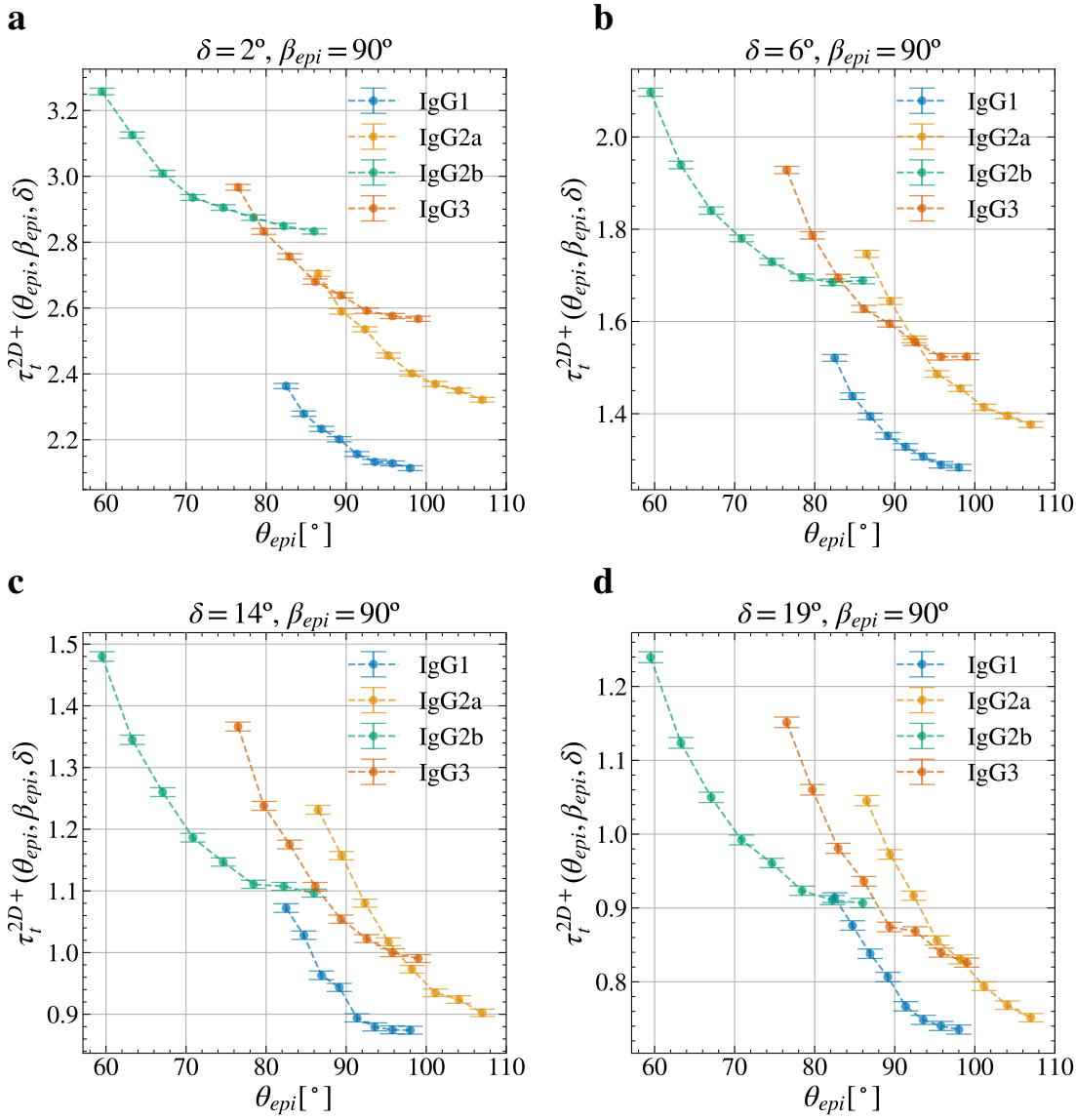

Figure 7: **Isotype Fab tilt flexibility affects the effective orientational rates**. MFPT $\tau_t^{2D+}(\theta_{\text{epi}}, \beta_{\text{epi}}, \delta)$ computed through Monte-Carlo simulations for the different mouse IgGs subclasses and multiples values of θ_{epi} and δ keeping fixed $\beta_{\text{epi}} = 90°$. Parameters : $dt = 2 \cdot 10^{-4}$, $D = 1$, # initial positions = 3000, # repetitions per initial position = 100. **a** to **d** correspond to paratope angles $\delta = 2° - 19°$.

$$\tau_t^{2D+}(\delta) = \frac{\log\left(\frac{\tan\frac{\hat{\theta}_{\max}}{2}}{\tan\frac{\delta}{4}}\right) + \cos\hat{\theta}_{\max}\left[1 + \log\left(\frac{\cos^2\frac{\delta}{4}\sin\frac{\delta}{2}}{\cos^2\frac{\hat{\theta}_{\max}}{2}\sin\hat{\theta}_{\max}}\right) + (1 - \cos\hat{\theta}_{\max})\log\left(\frac{\tan\frac{\delta}{4}}{\tan\frac{\hat{\theta}_{\max}}{2}}\right)\right] - \cos\frac{\delta}{2}}{D\left(\cos\delta/2 - \cos\hat{\theta}_{\max}\right)} \tag{25}$$

where $D = D_t$. The resulting on rate is given by

$$e_t^{2D+} = \frac{1}{\tau_t^{2D+}} \tag{26}$$

Figure 8b shows the estimated global MFPT $\tau_t^{2D+}(\delta)$ of the IgGs subclasses averaged over the different positions of θ_{epi} and a non-linear least square fitting to Eqn. (25) with respect to the free parameter $\hat{\theta}_{\max}$. The fitted values of $\hat{\theta}_{\max}$ correlate linearly with the angle difference $\theta_{\max}^{2D} - \theta_{\min}^{2D}$ ($R^2 = 0.98$, $\hat{\theta}_{\max} = 0.44\,(\theta_{\max}^{2D} - \theta_{\min}^{2D}) + 45°$).

The off-rate process for BCRs is similar to that of soluble Abs with the exception that the whole rotational motion marginally contributes to the diffusion of the paratope. Therefore, the rotation off-rate $e_{t+w}^{2D-}(\delta) \approx e_t^{2D-}(\delta)$ is given as Eqn. (22) by:

$$e_t^{2D-}(\delta) \approx \frac{8D_t}{\sin^2 \delta/2}. \tag{27}$$

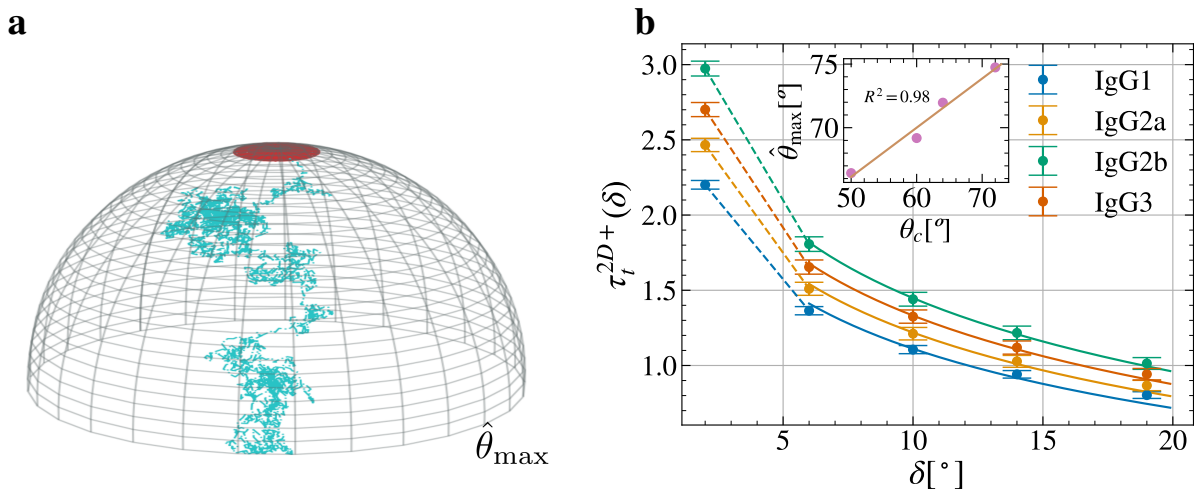

Figure 8: **Variational Global MFPT approximation of $\tau_{t+w}^{2D+}(\delta)$.** **a**, As an approximation of BCR's paratope diffusion process (Fig. 6), we considered the case where the epitope is at one of the poles and the paratope can diffuse in a polar cap of size $\hat{\theta}_{\max}$. **b,** Global MFPT $\tau_{t+w}^{2D+}(\delta)$ for the IgGs subclasses. Single points are the computed global MFPT $\tau_{t+w}^{2D+}(\delta)$, which result from averaging $\tau_{t+w}^{2D+}(\theta_{\text{epi}}, \beta_{\text{epi}}, \delta)$ of Fig. 7 over θ_{epi}. Solid lines are given by a non-linear least square fitting to Eqn. (25). Inset shows the values of the fitted $\hat{\theta}_{\max}$ against the difference $\theta_c = \theta_{\max} - \theta_{\min}$ of each IgGs subclasses. The point with $\delta = 2$ was not considered for the fitting due to its unfeasibility in real epitopes. Values of $\hat{\theta}_{\max}$: $\hat{\theta}_{\max}^{IgG1} = 66.4°$, $\hat{\theta}_{\max}^{IgG2a} = 69.1°$, $\hat{\theta}_{\max}^{IgG2b} = 74.7°$, $\hat{\theta}_{\max}^{IgG3} = 72.0°$.

ESTIMATES FOR THE RATE CONSTANTS $k_d^{\pm}$ AND $e^{\pm}$ IN 2D AND 3D, AND THE CORRESPONDING k^+ THRESHOLD VALUES

In order to see the empirical impact of Eqns. (3) to estimate the true underlying kinetic rates, here we integrate all the computations in the preceding sections. In particular, to estimate the rate constants $e^{\pm}$ it is necessary to know, in addition to the angles ϕ_0 and δ, the rotational diffusion constants D_a, D_t and D_w in 2D and 3D conditions. These diffusion constants can be calculated as follows. The mean square angular

deviation of a rotating molecule after a time t is given by (23, 29)

$$\langle \phi^2 \rangle = c\, D\, t \quad \text{(in units } rad^2\text{)},$$

where c is a constant particular for the geometry of the rotation, and D is the corresponding rotational diffusion constant. In particular, $c = 2$ for Fab twist and BCR Fc axial rotations, and $c = 6$ for Fab tilt and whole Ab rotations (8, 30). For such rotations, the mean rotational correlation time, denoted $t_{1\text{rad}}$, is the average time spent by the molecule to rotate 1 rad. Therefore,

$$D = \frac{1\ \text{rad}^2}{c\ t_{1\text{rad}}}.$$

The values for $t_{1\text{rad}}$ corresponding to the three rotations considered here (whole molecule, tilt and alignment) and/or the respective rotational diffusion constants, D_w, D_t and D_a, estimated for Igs both in solution (3D) and attached to a large particle (2D) are summarized in Table 3. In addition, and as previously mentioned, although D_w(2D) for the rotation of BCRs about the Fc axis has not been determined, one can take as a reference value that of the epidermal growth factor receptor (23), $D_w(2\text{D}) \approx 1.43 \times 10^3$ rad^2/s.

Calculations for k_d^+ and k_d^- can be found in (8). The global rotational kinetic rates, e^+ and e^-, can now be calculated applying the estimations for the rotational diffusion constants in Table 3 and for the angles ϕ_0 and δ (given at the end of section **Mathematical derivation of the rotational rates**) to Eqns. (12), (18), (22), (25), and then applying the resulting values to Eqns. (6). Ranges for the translational and global rotational kinetic rates in 2D and 3D conditions thus estimated, together with the corresponding threshold values for k^+ given by Eqn. 4, are summarized in Table 4.

These estimates have a huge impact on our understanding of the underlying kinetics. For instance, if $k^+ > k^+_{\text{threshold}}$ then the effective *on* rate becomes independent of k^+ and approaches a *plateau* rate, $k^+_{\text{eff}} \rightarrow k^+_{\text{plateau}}$.

Calculations of the theoretical limits for the 3D k^+_{eff} of Ab-Ag interactions (Fig. 9**a**) help to explain the long-made empirical observation of a ceiling for the k^+_{eff} of monoclonal Abs and their ligands. For instance, in Fig. 9b we illustrate this effect using the experimental data in Ref. (31). Interestingly, while k_d^+ and k_d^- have mathematical similar scaling factors ($\sim 10^3$-fold) from 2D to 3D conditions, e^+ and e^- have have similar values in 2D and 3D conditions (with e^- being 2-fold lower in 2D than in 3D). However, what is relevant here is that the k^+ threshold values differ by $\sim 10^3$-fold from 2D to 3D conditions. Hence, the plateau for BCR-Ag k^+_{eff} rates is much lower than for free Ab-Ag interactions. More specifically, the k^+ threshold in 2D is about 10^6 s^{-1} and there. Therefore, 3D Ab-Ag effective affinity constants cannot be used as surrogates for 2D BCR-Ag effective affinity constants.

DISCUSSION AND CONCLUSIONS

It is somewhat surprising that despite the widespread use of the seminal works by Berg and Purcell (15) and De Lisi (14), there has been put so little emphasis on the understanding of one of the central actors in the

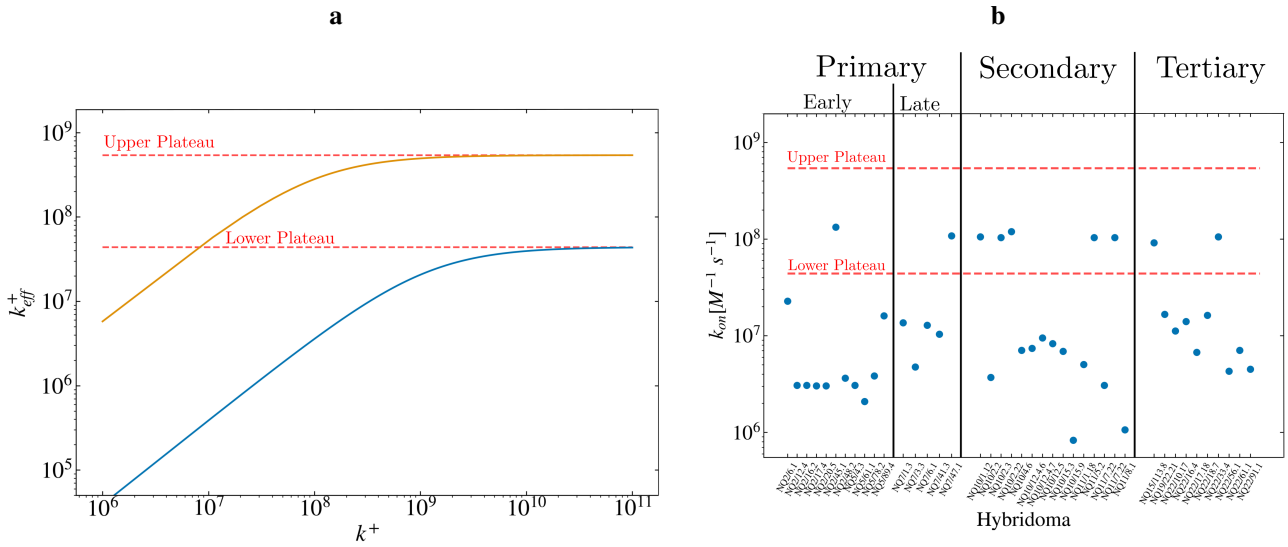

Figure 9: **Translational and rotational diffusion events limit the ability to estimate *on*-rates**. **a**, Equation(2) vs the true (underlying) binding rate, k^+, applied to the interaction of free Abs with their Ags. The rectangle represents the estimated range for k^+_{plateau} using the data in Table 4 for 3D interactions. **b**, Experimental data using monoclonal Abs and their Ags (31). Note the close agreement between the experimental data and our predicted plateau above which the true (underlying) *on* rate cannot be measured. To overcome these limitations, the experimental setup must control for translational and rotational events. Parameters for lower plateau: $k^+_d = 3.8 \cdot 10^8$ M^{-1} s^{-1}, $k^-_d = 7.2 \cdot 10^6$ s^{-1}, $e^+ = 9.4 \cdot 10^5$ s^{-1} and $e^- = 1.27 \cdot 10^9$ s^{-1}. Parameters for upper plateau: $k^+_d = 3.4 \cdot 10^9$ M^{-1} s^{-1}, $k^-_d = 7.2 \cdot 10^6$ s^{-1}, $e^+ = 1.36 \cdot 10^6$ s^{-1} and $e^- = 1.1 \cdot 10^8$ s^{-1}.

Table 3: Mean rotational correlation times of IgG molecules and D_t and D_a diffusion constants.

	3D[a]					
	Whole Ig rotation		**Fab tilt**		**Fab alignment**	
Ig isotype	$t_{1\text{rad}}$ ($\times 10^{-9}$ s)	D_w ($\times 10^{6}$ rad^2/s)	$t_{1\text{rad}}$ ($\times 10^{-9}$ s)	D_t ($\times 10^{6}$ rad^2/s)	$t_{1\text{rad}}$ ($\times 10^{-9}$ s)	D_a ($\times 10^{7}$ rad^2/s)
IgG2b[b]	–	–	47	3.5	–	–
IgG2a[b]	–	–	60	2.8	–	–
IgG1[b]	–	–	81-93	2.1-1.8	–	–
IgE[b]	–	–	124	1.3	–	–
IgG[c]	158	1.1	83-103	2.0-1.6	14-18	3.6-2.8
IgG[d]	–	0.7	–	–	–	–
	2D[a]					
	Whole BCR rotation		**Fab tilt**		**Fab alignment**	
	$t_{1\text{rad}}$	D_w	$t_{1\text{rad}}$ ($\times 10^{-9}$ s)	D_t ($\times 10^{6}$ rad^2/s)	$t_{1\text{rad}}$ ($\times 10^{-9}$ s)	D_a ($\times 10^{7}$ rad^2/s)
IgG[c]	–	–	140-150	1.2-1.1	10-16	5.0-3.1

[a]3D values estimated from IgG molecules in saline solution(24, 32); 2D values estimated from IgG molecules attached to a large particle (33).

[b]Mouse monoclonal antibodies; $t_{1\text{rad}}$ data from (24).

[c]Purified rabbit polyclonal total IgG; $t_{1\text{rad}}$ data from (32, 33).

[d]Purified bovine polyclonal total IgG; D_w data from (34).

Table 4: Estimated ranges of translational and rotational diffusion rate constants for Igs in 2D and 3D conditions, and the corresponding threshold values for k^+.

	Translational diffusion		Rotational diffusion		Threshold
	k_d^+	k_d^-	e^+	e^-	$\frac{k_d^- e^-}{(k_d^- + e^+)}$
2D Isotype	($\times 10^5$ M^{-1} s^{-1})	($\times 10^2$ s^{-1})	($\times 10^5$ s^{-1})	($\times 10^8$ s^{-1})	($\times 10^5$ s^{-1})
IgG1	8.8–29	8.3–27	11.6–14.7	3.2–4.9	1.8–11.5
IgG2a			10.6–13.4		2.0-12.5
IgG2b			9.0–11.2		2.4–14.8
IgG3			9.7–12.2		2.2–13.7
3D Isotype	($\times 10^8$ M^{-1} s^{-1})	($\times 10^5$ s^{-1})	($\times 10^5$ s^{-1})	($\times 10^8$ s^{-1})	($\times 10^8$ s^{-1})
IgG	3.8–34	5.3–72	9.4–13.6	6.7–12.7	1.9–11

humoral immune response: B-cell receptors and antibodies. Here, we have extended previous works (7, 8) to emphasize that, as it has already been acknowledged for TCRs (35, 36), BCR-Ag binding kinetics cannot be inferred from their Ab-Ag counterparts. Specifically, the microscopic degrees of freedom (beyond pure spatial diffusion) and the mechanical properties of the Ab/BCR (flexibility) must be carefully and systematically analyzed to quantify) the impact on the effective rates, which, depending on the experimental setup, is the only observable information.

Here we have used the Narrow escape theory (11), and first passage processes (12) to determine the parametric dependence of *on* and *off* rates on the structural properties of both BCRs and Abs. We have characterized every step entailing the rotational degrees of freedom so we can use the most precise available empirical estimates. In that regard, we have also thoroughly surveyed the existing literature to extract those quantitative estimates. This has been a paramount task as empirical studies are scarce, they are performed with different types of antibodies so we expect that new targeted studies will, indeed, narrow our estimates.

Our results show that this dissection is not a mere academic exercise but, as illustrated for instance in Figs. 7 or 9, it has deep practical implications. To name a few, whether one can extrapolate SPR assays to actual B-cell activation in the germinal center; the role of isotypes in the binding kinetics; or the practical relevance of having different k^+ thresholds for 2D BCR-Ag vs. 3D Ab-Ag binding kinetics. Also, as shown in Tables.3 and 4, the orders of magnitude of some of the individual events (tilt, whole rotation or alignment) are of the same order of magnitude as the actual binding rates.

Our calculations aim to catalyze experimental studies to determine the differences between Ab-Ag and BCR-Ag kinetics and encourage using state-of-the-art molecular dynamics simulations and experimental methods to narrow the estimated rates for some of the aforementioned rotational events.

In summary, and paraphrasing Malissen and Bongrand (37), a B cell can make decisions only based on parameters it senses, not on quantities measured *in vitro* by experimentalists. We have shown that contrary to the traditional implicit assumption: the kinetics of BCR-Ag interactions cannot be inferred, in general, from those of Ab-Ag interactions. This has important implications in interpreting observations related to the germinal center (GC) reaction, an essential process in T-dependent humoral responses.

AUTHOR CONTRIBUTIONS

MGS performed all the Montecarlo simulations. All of the authors contributed equally to the rest of tasks.

ACKNOWLEDGMENTS

This work has been partially funded by MCIN/AEI/ 10.13039/501100011033, through Grants PID2019-106339GB-I00, and PRE2020-092274, and by “ESF Investing in your future”, and by Xunta de Galiza under project GRC-ED431C 2020/02.

REFERENCES

1. Punt, J., S. Stranford, P. Jones, and J. Owen, 2019. Kuby immunology. Macmillan Education, New York, 8th edition.

2. Casadevall, A., and A. Janda, 2012. Immunoglobulin isotype influences affinity and specificity. *Proc Natl Acad Sci U S A* 109:12272–3.

3. Roux, K. H., L. Strelets, and T. E. Michaelsen, 1997. Flexibility of human IgG subclasses. *The Journal of Immunology* 159:3372–3382. https://www.jimmunol.org/content/159/7/3372.

4. Szakal, A., M. Kosco, and J. Tew, 1988. A novel in vivo follicular dendritic cell-dependent iccosome-mediated mechanism for delivery of antigen to antigen-processing cells. *The Journal of Immunology* 140:341–353.

5. Heesters, B. A., P. Chatterjee, Y.-A. Kim, S. F. Gonzalez, M. P. Kuligowski, T. Kirchhausen, and M. C. Carroll, 2013. Endocytosis and Recycling of Immune Complexes by Follicular Dendritic Cells Enhances B Cell Antigen Binding and Activation. *Immunity* 38:1164–1175. https://www.sciencedirect.com/science/article/pii/S1074761313002367.

6. Heath, W. R., Y. Kato, T. M. Steiner, and I. Caminschi, 2019. Antigen presentation by dendritic cells for B cell activation. *Curr Opin Immunol* 58:44–52.

7. Faro, J., M. Castro, and C. Molina-París, 2017. A unifying mathematical framework for experimental TCR-pMHC kinetic constants. *Scientific Reports* 7:46741.

8. Faro, J., and M. Castro, 2021. Affinity Selection in Germinal Centers: Cautionary Tales and New Opportunities. *Cells* 10:1040. https://doi.org/10.3390%2Fcells10051040.

9. Limozin, L., P. Bongrand, and P. Robert, 2016. A Rough Energy Landscape to Describe Surface-Linked Antibody and Antigen Bond Formation. *Sci Rep* 6:35193.

10. González, C., P. Chames, B. Kerfelec, D. Baty, P. Robert, and L. Limozin, 2019. Nanobody-CD16 Catch Bond Reveals NK Cell Mechanosensitivity. *Biophys J* 116:1516–1526.

11. Holcman, D., and Z. Schuss, 2015. Stochastic narrow escape in molecular and cellular biology. *Analysis and Applications. Springer, New York* .

12. Redner, S., 2001. A guide to first-passage processes. Cambridge University Press.

13. Arnold, J. N., M. R. Wormald, R. B. Sim, P. M. Rudd, and R. A. Dwek, 2007. The impact of glycosylation on the biological function and structure of human immunoglobulins. *Annu Rev Immunol* 25:21–50.

14. Delisi, C., 1981. The effect of cell size and receptor density on ligand-receptor reaction rate constants. *Molecular immunology* 18:507–511.

15. Berg, H. C., and E. M. Purcell, 1977. Physics of chemoreception. *Biophysical Journal* 20:193–219. https://www.sciencedirect.com/science/article/pii/S0006349577855446.

16. Saphire, E. O., R. L. Stanfield, M. M. Crispin, P. W. Parren, P. M. Rudd, R. A. Dwek, D. R. Burton, and I. A. Wilson, 2002. Contrasting IgG Structures Reveal Extreme Asymmetry and Flexibility. *Journal of Molecular Biology* 319:9–18. https://doi.org/10.1016%2Fs0022-2836%2802%2900244-9.

17. Løset, G. Å., K. H. Roux, P. Zhu, T. E. Michaelsen, and I. Sandlie, 2004. Differential Segmental Flexibility and Reach Dictate the Antigen Binding Mode of Chimeric IgD and IgM: Implications for the Function of the B Cell Receptor. *The Journal of Immunology* 172:2925–2934. http://dx.doi.org/10.4049/jimmunol.172.5.2925.

18. Wrigley, N., E. Brown, and J. Skehel, 1983. Electron microscopic evidence for the axial rotation and inter-domain flexibility of the fab regions of immunoglobulin G. *Journal of Molecular Biology* 169:771–774. https://doi.org/10.1016%2Fs0022-2836%2883%2980170-3.

19. Wade, R., J. Taveau, and J. Lamy, 1989. Concerning the axial rotational flexibility of the Fab regions of immunoglobulin G. *Journal of Molecular Biology* 206:349–356. https://doi.org/10.1016%2F0022-2836%2889%2990484-1.

20. Schlosshauer, M., and D. Baker, 2004. Realistic protein-protein association rates from a simple diffusional model neglecting long-range interactions, free energy barriers, and landscape ruggedness. *Protein Science* 13:1660–1669. https://doi.org/10.1110%2Fps.03517304.

21. Reth, M., 2013. Matching cellular dimensions with molecular sizes. *Nature immunology* 14:765.

22. Ramaraj, T., T. Angel, E. A. Dratz, A. J. Jesaitis, and B. Mumey, 2012. Antigen-antibody interface properties: Composition, residue interactions, and features of 53 non-redundant structures. *Biochimica et Biophysica Acta (BBA) - Proteins and Proteomics* 1824:520–532. https://doi.org/10.1016%2Fj.bbapap.2011.12.007.

23. Schlessinger, J., 1983. Lateral and rotational diffusion of EGF–receptor complex: Relationship to receptor-mediated endocytosis. *Biopolymers* 22:347–353. http://dx.doi.org/10.1002/bip.360220145.

24. Oi, V. T., T. M. Vuong, R. Hardy, J. Reidler, J. Dangl, L. A. Herzenberg, and L. Stryer, 1984. Correlation between segmental flexibility and effector function of antibodies. *Nature* 307:136–140. http://dx.doi.org/10.1038/307136a0.

25. Zhang, X., L. Zhang, H. Tong, B. Peng, M. J. Rames, S. Zhang, and G. Ren, 2015. 3D Structural Fluctuation of IgG1 Antibody Revealed by Individual Particle Electron Tomography. *Scientific Reports* 5:9803. http://www.nature.com/articles/srep09803.

26. Hussain, R., G. Dawood, N. Abrar, Z. Toossi, A. Minai, M. Dojki, and J. J. Ellner, 1995. Selective increases in antibody isotypes and immunoglobulin G subclass responses to secreted antigens in tuberculosis patients and healthy household contacts of the patients. *Clinical and Diagnostic Laboratory Immunology* 2:726–732. https://cvi.asm.org/content/2/6/726.

27. Golding, B., 1991. Cytokine regulation of humoral immune responses. Topics in vaccine adjuvant research. CRC Press.

28. de Haan, N., D. Falck, and M. Wuhrer, 2020. Monitoring of immunoglobulin N- and O-glycosylation in health and disease. *Glycobiology* 30:226–240.

29. Saffman, P., and M. Delbrück, 1975. Brownian motion in biological membranes. *Proceedings of the National Academy of Sciences* 72:3111–3113.

30. Stingaciu, L. R., O. Ivanova, M. Ohl, R. Biehl, and D. Richter, 2016. Fast antibody fragment motion: flexible linkers act as entropic spring. *Scientific Reports* 6. https://doi.org/10.1038%2Fsrep22148.

31. Foote, J., and C. Milstein, 1991. Kinetic maturation of an immune response. *Nature* 352:530–532. http://www.ncbi.nlm.nih.gov/pubmed/1907716.

32. Hanson, D. C., J. Yguerabide, and V. N. Schumaker, 1981. Segmental flexibility of immunoglobulin G antibody molecules in solution: a new interpretation. *Biochemistry* 20:6842–6852. https://doi.org/10.1021%2Fbi00527a016.

33. Hanson, D. C., J. Yguerabide, and V. N. Schumaker, 1985. Rotational dynamics of immunoglobulin G antibodies anchored in protein a soluble complexes. *Molecular Immunology* 22:237–244. https://doi.org/10.1016%2F0161-5890%2885%2990156-7.

34. Grimaldo, M., F. Roosen-Runge, F. Zhang, T. Seydel, and F. Schreiber, 2014. Diffusion and Dynamics of γ-Globulin in Crowded Aqueous Solutions. *The Journal of Physical Chemistry B* 118:7203–7209. https://doi.org/10.1021%2Fjp504135z.

35. Huang, J., V. Zarnitsyna, B. Liu, L. Edwards, N. Jiang, B. Evavold, and C. Zhu, 2010. The kinetics of two dimensional TCR and pMHC interactions determine T cell responsiveness. *Nature* 464:932.

36. Huppa, J., M. Axmann, M. Mörtelmaier, B. Lillemeier, E. Newell, M. Brameshuber, L. Klein, G. Schütz, and M. Davis, 2010. TCR–peptide–MHC interactions in situ show accelerated kinetics and increased affinity. *Nature* 463:963–967.

37. Malissen, B., and P. Bongrand, 2015. Early T cell activation: integrating biochemical, structural, and biophysical cues. *Annu Rev Immunol* 33:539–61.

38. Novikov, A., D. Kuzmin, and O. Ahmadi, 2020. Random walk methods for Monte Carlo simulations of Brownian diffusion on a sphere. *Applied Mathematics and Computation* 364:124670. https://linkinghub.elsevier.com/retrieve/pii/S0096300319306629.

Methods

Algorithm 1 Diffusion on the sphere

function DIFFUSION(dt, $\vec{r}$, Ω_a, Ω_r)
  t $\leftarrow 0$
  while $\vec{r} \notin \Omega_a$ **do**
    $t \leftarrow t + dt$
    $\vec{\delta_r} \leftarrow (0,0,1) + \sqrt{2dt}\ (\xi_1(t), \xi_2(t), 0)$
    $\vec{\delta_r} \leftarrow \vec{\delta_r}/\|\vec{\delta_r}\|_2$
    $(\theta, \phi) \leftarrow$ Spherical coordinates of $\vec{r}$
    $\vec{r} \leftarrow$ Rotate $\vec{\delta_r}$ by θ and ϕ
    if $\vec{r} \notin \Omega_r$ **then**
      $\vec{r} \leftarrow$ Reflect $\vec{r}$
    end if
  end while
  return t
end function

Monte-Carlo simulations of Brownian motion on the sphere were performed with the algorithm of projecting cartesian random walks (38) (see 1 for an algorithm's pseudo-code). Starting over a random point $p_0 = (\theta_0, \phi_0)$ of the spherical domain Ω, the algorithm produces a cartesian random walk on the tangential plane to the north pole. The endpoint of the random walk $\delta(x, y, z)$ is projected back onto the sphere $\delta(x, y, z)/\|\delta(x, y, z)\|^2$ and converted to spherical coordinates $\delta(\theta, \phi)$. The following point of the random walk on Ω is obtained by applying a rotation $\hat{R}$ of angles θ_0 and ϕ_0 to $\delta(\theta, \phi)$, i.e, $p_1(\theta_1, \phi_1) = \hat{R}(\theta_0, \phi_0)\delta(\theta, \phi)$. If the new point $p_1(\theta_1, \phi_1)$ surpass the reflecting boundary $\partial\Omega_r$ is orthogonally reflected with respect to the boundary. The random walk on Ω continues until it arrives at the absorbing domain Ω_a.

A Python implementation of the algorithm is available at the following public repository: https://github.com/MiguelGarciaSanchez/First-Passage